On the Wafer/Pad Friction of Chemical–Mechanical Planarization (CMP) Processes—Part I: Modeling and Analysis

Jingang Yi, *Member, IEEE*

***Abstract*—Friction characteristics between the wafer and the polishing pad play an important role in the chemical–mechanical planarization (CMP) process. In this paper, a wafer/pad friction modeling and monitoring scheme for the linear CMP process is presented. Kinematic analysis of the linear CMP system is investigated and a distributed LuGre dynamic friction model is utilized to capture the friction forces generated by the wafer/pad interactions. The frictional torques of both the polisher spindle and the roller systems are used to monitor *in situ* the changes of the friction coefficient during a CMP process. Effects of pad conditioning and patterned wafer topography on the wafer/pad friction are also analyzed and discussed. The proposed friction modeling and monitoring scheme can be further used for real-time CMP monitoring and process fault diagnosis.**

***Index Terms*—Chemical–mechanical planarization (CMP), friction, LuGre friction model, process modeling and monitoring, shallow trench isolation (STI).**

I. Introduction

CHEMICAL–MECHANICAL planarization (CMP) is an important enabling technology for semiconductor manufacturing. During a CMP process, the wafer is pushed down against a moving polishing pad to achieve surface planarization. Chemical slurry is poured onto the polishing pad to assist the material removal and surface planarization. It is widely known that the chemical reactions between slurry fluids and the wafer surface and mechanical abrasiveness between particles in slurry and the wafer surface aid material removal during the polishing process. Slurry fluids also help to remove the ground-off materials and byproducts.

Due to the complexity of the process environments and lack of *in situ* sensors, the CMP process is not completely understood. In recent years, various mathematical models were developed to explain the material removal mechanisms assuming different wafer/pad contact regimes. These wafer/pad contact regimes can be categorized as direct contact, semi-direct contact, and lubrication and hydrodynamic contact. For example, Wang *et al.* [1] and Fu *et al.* [2] used a solid-to-solid contact mechanics model to explain the material removal. In Runnels and Eyman [3], Sundararajan *et al.* [4], and Cho *et al.* [5], hydrodynamic and lubrication models were proposed assuming that there exists a slurry fluid film between the wafer and the polishing pad. Based on a lubrication and mass transport model, Thakurta *et al.* [6] also considered the deformation of the pad. An idealized model of a mixture of contact mechanics and lubrication hydrodynamics was discussed in Tichy *et al.* [7] with some geometry assumptions.

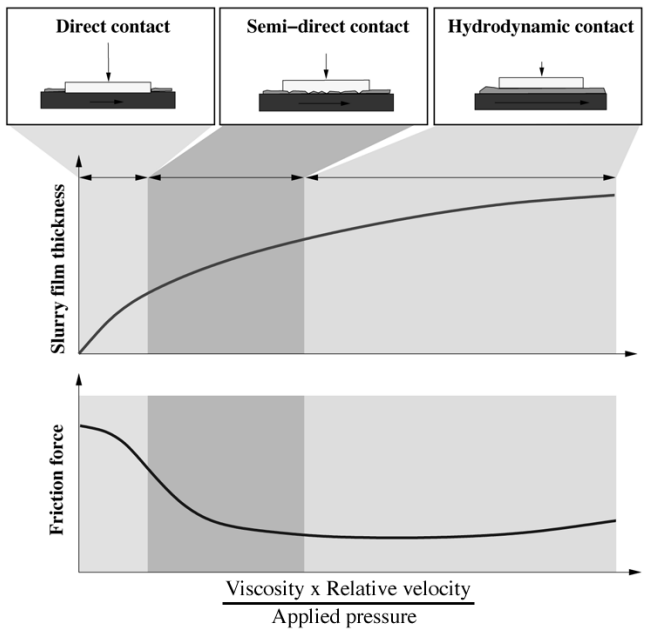

Fig. 1. Schematic of slurry thin film thickness, friction force, and different water/pad contact regimes for CMP processes.

It has been generally assumed that the thickness of the thin slurry film between the wafer and the pad determines which regime a particular process setup belongs to. Fig. 1 shows the relationship among various contact regimes, slurry film thickness, and some polishing parameters, such as slurry viscosity, relative velocity between the wafer and the polishing pad, and applied wafer/pad pressure [8].

The characteristics of the wafer/pad interface play an important role in the CMP process performance. In this two-part paper [9], we discuss one important mechanical characteristic of such an interface: wafer/pad friction. Direct and semi-direct wafer/pad contact regimes are considered in this study since they have been observed in most CMP processes [2], [7]. Fig. 1 shows the change of the friction force under various CMP regimes. Investigation of wafer/pad friction in CMP processes is first discussed as a method for automatic process end-point

Manuscript received May 27, 2004; revised March 4, 2005.

The author was with Lam Research Corporation, Fremont CA 94538 USA. He is now with the Department of Mechanical Engineering, Texas A&M University, College Station, TX 77843 USA (e-mail: jgyi@tamu.edu).

Digital Object Identifier 10.1109/TSM.2005.852101

0894-6507/$20.00 © 2005 IEEE

detection (EPD). For a good review of friction EPD for CMP processes, readers can refer to Bibby and Holland [10], Hetherington and Stein [11], and references therein. Litvak and Tzeng [12] discussed briefly the use of the spindle motor current for EPD and process monitoring. Sikder *et al.* [13] discussed measuring the coefficient of friction (COF) under various polishing parameters such as table rotating speed and polishing downforce on a prototype of a rotary CMP polisher without pad conditioning. Recently, Homma *et al.* [14] showed that the CMP material removal rate is proportional to the wafer/pad friction force.

All of the aforementioned literature discussed either empirical or experimental approaches to study wafer/pad friction with some simplified processes. For a multistep CMP process, polishing parameters could change from step to step and, therefore, the friction force or torque could vary accordingly. In order to monitor *in situ* the friction changes and use this information to further enhance the process performance, we need to understand the underlying physics and the relationship between the polishing parameters and the measured friction forces. The recently developed Cu/low-k CMP processes require real-time friction monitoring. However, there are few studies on the actual wafer/pad friction mechanism and on how to monitor the wafer/pad friction *in-situ*. One of the main goals of this study is to fill such a gap. Particularly, we investigate: 1) the distributed friction forces across the wafer/pad contact surface; 2) the impacts of pad conditioning and wafer film topography on wafer/pad friction; and 3) estimating and monitoring the friction coefficient under various polishing conditions and relevant applications. Although the linear CMP polisher is used as an example for modeling and analysis, the analysis and results can be extended and applied to any other orbital and rotary CMP polishers.

The remainder of this paper is organized as follows. Section II describes the Lam linear planarization technology (LPT) CMP systems including the pad conditioning systems. In Section III, we present a wafer/pad friction model without considering the pad conditioning effect. Friction torques applied on both spindle and roller systems are discussed. The pad conditioning effect on wafer/pad friction is investigated in Section IV. Section V discusses the effect of wafer pattern topography on the wafer/pad friction characteristic. Concluding remarks are presented in Section VI.

II. Linear CMP

During a CMP process, the wafer is held face-down with air suction by a wafer carrier against the polishing pad. In widely-used rotary CMP polishers, the polishing pad is on a rotating table with a relatively large radius. The wafer carrier is rotating against the polishing pad table. The polishing pad table is normally rigid, and the wafer carrier can be tilted or controlled by the inside air zones.

The linear polisher uses a different mechanism. Fig. 2 shows a schematic of the Lam LPT setup. The polishing pad is moving linearly against the rotating wafer. An air-bearing supports the polishing pad from an air platen underneath the pad [see Fig. 3(a)]. The air zones on the platen are a set of co-centered

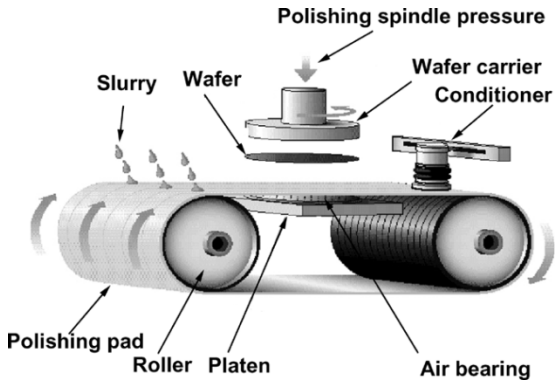

Fig. 2. Schematic of Lam linear CMP systems.

small holes located at different radii as shown in Fig. 3(b). By tuning the air pressure of different air zones on the platen and adjusting platen height, we can change the polishing pad deformation and therefore control the wafer polishing uniformity. The use of this proprietary air-bearing platen intrinsically improves within-wafer nonuniformity (WIWNU) and decouples uniformity control from removal rate and planarization control. Compared with regular rotary CMP tools, the LPT design can provide a wide range of polishing pad speeds and polishing pressures, and, therefore, increases the process throughput, as well as the planarization performance [15].

In CMP processes, it is critial that the surface of the polish pad is maintained at a certain roughness level in order to keep the process performance stable. Conditioning the pad is an effective method to achieve this [16]. In practice, a moving abrasive conditioning disk is pushed against the moving polish pad with controllable contact force. Hundreds of small diamonds are usually mounted on the conditioner disk surface. When the disk is moving across the pad, it will scratch the pad and, therefore, maintain the pad surface roughness level. Fig. 4 shows two different pad conditioning systems: radial arm and linear. For the radial arm conditioner system [Fig. 4(a)], the conditioner disk is driven by a rotating arm at a constant angular speed. The linear conditioner instead moves in a straight line across the polishing pad. We will discuss the kinematics of the conditioner system in Section IV.

III. Friction Model Without Pad Conditioning

The friction force between the wafer and the polishing pad during a polishing process is highly dependent on the relative velocity distribution and the wafer/pad surface characteristics. In this section, we discuss the friction modeling without considering the pad conditioning effect.

The polishing pad normally is made of layers of polyurethane. During polishing, it is believed that the wafer is supported by the pad pores [7], [17]. On the polishing pad surface, there are a lot of broken pores (from pad conditioning) and slurry can then accumulate inside these pores. When a wafer is pushed against the pad, some slurry particles are squeezed into the pad pores and remove the wafer film. Fig. 5 shows a scanning electron microscopy (SEM) picture of the pad cross section and a schematic of the wafer/pad contact.

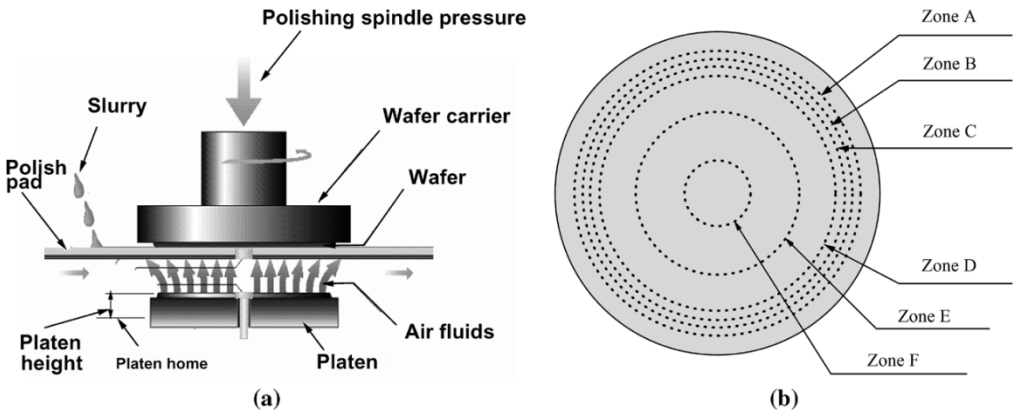

Fig. 3. LPT air-bearing systems. (a) Polishing platen assembly. (b) Platen air zones.

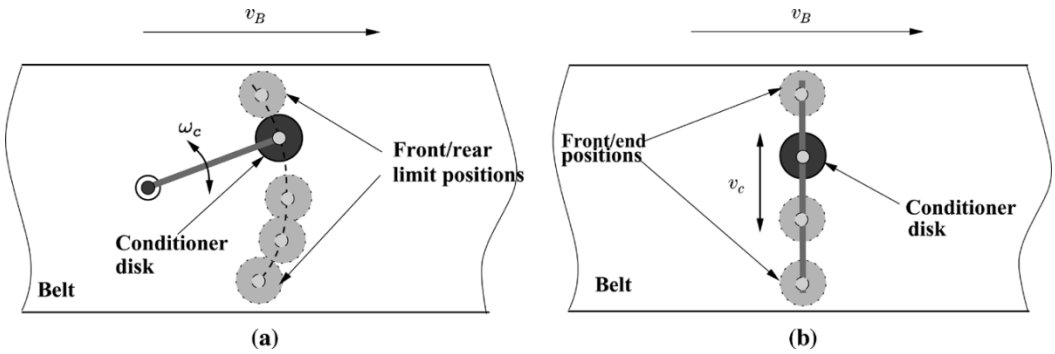

Fig. 4. LPT conditioner systems. (a) Radial arm conditioner. (b) Linear conditioner.

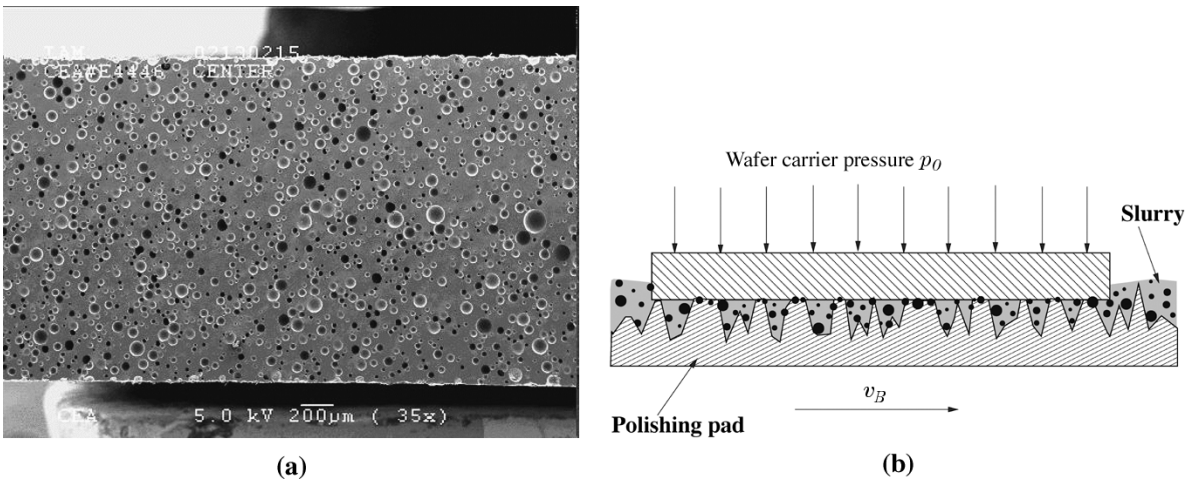

Fig. 5. (a) SEM picture of IC 1000 pad cross section. (b) Schematic of wafer/pad contact.

A. Friction Force and Spindle Torque

In the following, we first investigate the kinematic relationship between the wafer and polishing pad and then study the friction forces and torques. Fig. 6 shows a schematic of a polishing wafer on the moving polishing pad. Denote the polishing pad velocity as v_B and the wafer rotating speed as ω. For an arbitrary point A on the wafer surface, we can write the position vector $\mathbf{r}$ in the x-y coordinate system as

$$\mathbf{r} = (r\cos\phi)\mathbf{i} + (r\sin\phi)\mathbf{j}$$

where r is the distance from point A to the origin O, ϕ is the angle between vector $\overrightarrow{OA}$ and the x-axis, and $\mathbf{i}$ and $\mathbf{j}$ are the x, y unit vectors, respectively.

From Fig. 6, we can calculate the relative velocity $\mathbf{v}_{\rm rel}$ of the point A on the wafer with respect to the contacting point on the pad

$$\mathbf{v}_{\rm rel} = \mathbf{v}_W - \mathbf{v}_B = \dot{\mathbf{r}} - v_B\mathbf{i} = (-\omega r\sin\phi - v_B)\mathbf{i} + (\omega r\cos\phi)\mathbf{j}$$

and its magnitude is

$$|\mathbf{v}_{\rm rel}| = \sqrt{\omega^2 r^2 + 2v_B\omega r\sin\phi + v_B^2}. \quad (1)$$

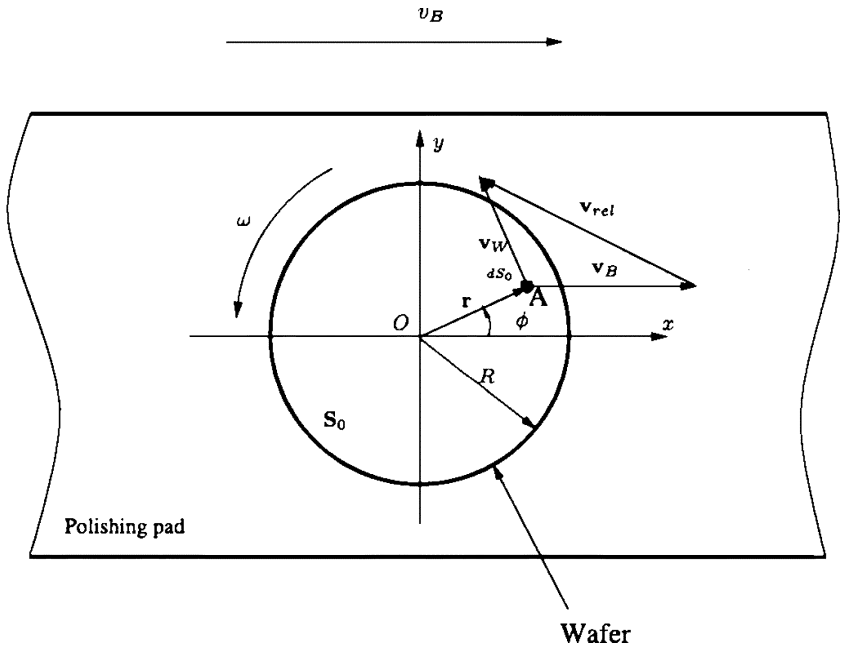

Fig. 6. Schematic of the linear CMP wafer/pad kinematic relationship.

Assume that for blanket wafers the average wafer/pad contact pressure p is uniformly distributed across the wafer and that p is equal to the external applied pressure p_0. For patterned wafers, the pressure p is, however, not equal to the external applied pressure p_0 due to the wafer topography. We will discuss the patterned wafer topography effect in Section V. Denote the whole wafer surface area as S_0. Consider a small piece of area dS_0 around the point A on the wafer. Using the distributed LuGre dynamic friction model [18], we can calculate the friction force $\delta\mathbf{F}$ on dS_0 as

$$\begin{cases} \frac{d\delta\mathbf{z}}{dt} = \mathbf{v}_{\rm rel} - \theta\frac{\sigma_0|\mathbf{v}_{\rm rel}|}{g(\mathbf{v}_{\rm rel})}\delta\mathbf{z} \\ \delta\mathbf{F} = (\sigma_0\delta\mathbf{z} + \sigma_1\delta\dot{\mathbf{z}} + \sigma_2\mathbf{v}_{\rm rel})\delta F_n \end{cases} \tag{2}$$

where $\delta\mathbf{z}$ is the average friction bristle deformation on dS_0, σ_i, $i = 0, 1, 2$, are the friction model parameters, and δF_n is the normal force applied on dS_0. The parameter θ is used to model the variations of the wafer/pad contact conditions. The function $g(\mathbf{v}_{\rm rel})$ is given by

$$g(\mathbf{v}_{\rm rel}) = \mu_c + (\mu_s - \mu_c)e^{-\frac{|\mathbf{v}_{\rm rel}|}{v_s}} \tag{3}$$

where μ_c and μ_s are the Coulomb and static friction coefficients between the wafer and pad surface, respectively, and v_s is the Stribeck velocity.

The LuGre friction model (2) uses the average microscopic bristle deformation $\delta\mathbf{z}$ to model the friction force $\delta\mathbf{F}$. The dynamics of $\delta\mathbf{z}$ is dependent on the relative velocity between two sliding surfaces. It has been demonstrated that the LuGre friction model accurately captures the friction characteristics between two contact surfaces [18], such as a wafer and polishing pad. Moreover, the model (2) has a simple mathematical form and is easily used for parameter estimation purposes.

For uniformly distributed pressure, $\delta F_n = p_0$. The total friction force $\mathbf{F}$ and spindle moment $\mathbf{M}^{\rm s}$[1] with respect to the wafer center O can be calculated as

$$\mathbf{F} = \int_{S_0} \delta\mathbf{F}dS_0, \quad \mathbf{M}^{\rm s} = \int_{S_0} \mathbf{r}\times\delta\mathbf{F}dS_0. \tag{4}$$

For the friction force model (2), the dynamic responses of the friction internal state $\delta\mathbf{z}$ are much faster than the polishing process dynamics. In a very short period of time, the friction force and moments have reached their steady-state values. We can, therefore, calculate the steady-state frictional moments by using the steady-state solutions of (2). Letting $(d\delta\mathbf{z}/dt) = 0$ in (2), we obtain

$$\delta\mathbf{z} = \frac{g(\mathbf{v}_{\rm rel})\mathbf{v}_{\rm rel}}{\theta\sigma_0|\mathbf{v}_{\rm rel}|} \quad\Longrightarrow\quad \delta\mathbf{F} = \left[\frac{g(\mathbf{v}_{\rm rel})}{\theta|\mathbf{v}_{\rm rel}|} + \sigma_2\right] p_0\mathbf{v}_{\rm rel}.$$

Substituting (4), we can calculate the friction moment $\delta\mathbf{M}^{\rm s}$ generated on dS_0 as

$$\begin{aligned} \delta\mathbf{M}^{\rm s} &= \mathbf{r}\times\delta\mathbf{F} = \left[\frac{g(\mathbf{v}_{\rm rel})}{\theta|\mathbf{v}_{\rm rel}|} + \sigma_2\right] p_0\mathbf{r}\times\mathbf{v}_{\rm rel} \\ &= p_0 r\left[\frac{g(\mathbf{v}_{\rm rel})}{\theta|\mathbf{v}_{\rm rel}|} + \sigma_2\right](\omega r + v_B\sin\phi)\mathbf{k} \end{aligned} \tag{5}$$

where $\mathbf{k} = \mathbf{i}\times\mathbf{j}$ is the unit vector along the z-axis.

In order to calculate the total moment applied on the spindle, we need to approximate the nonlinear function $g(\mathbf{v}_{\rm rel})$. Using a first-order approximation, from (3) we obtain

$$g(\mathbf{v}_{\rm rel}) \approx \mu_c + (\mu_s - \mu_c)\left(1 - \frac{|\mathbf{v}_{\rm rel}|}{v_s}\right) = \mu_s - (\mu_s - \mu_c)\frac{|\mathbf{v}_{\rm rel}|}{v_s}. \tag{6}$$

[1]We use superscript notations "s" and "r" to indicate the spindle and roller systems, respectively.

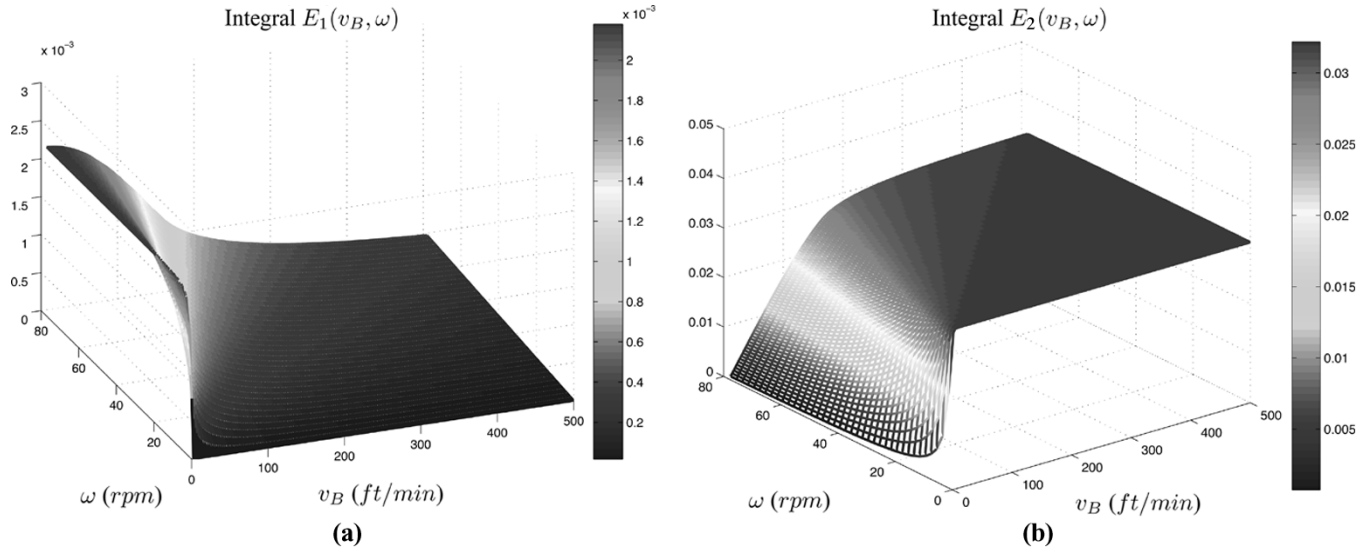

Fig. 7. Integral $E(v_B,\omega)$ as a function of the pad speed v_B and the wafer carrier rotating speed ω. (a) Integral $E_1(v_B,\omega)$. (b) Integral $E_2(v_B,\omega)$.

With the approximation (6), we can compute the friction moment (5) and obtain

$$\mathbf{M}^{\mathrm{s}} = \left(\int_{S_0} p_0 r \left[\frac{\mu_s}{\theta |\mathbf{v}_{\mathrm{rel}}|} + \sigma \right] (\omega r + v_B \sin\phi) dS_0 \right) \mathbf{k}$$

where $\sigma = \sigma_2 - (\mu_s - \mu_c / v_s \theta)$. The magnitude of the moment $|\mathbf{M}^{\mathrm{s}}|$ is calculated as

$$\begin{aligned} M^{\mathrm{s}} &= \int_{S_0} p_0 r \left[\frac{\mu_s}{\theta |\mathbf{v}_{\mathrm{rel}}|} + \sigma \right] (\omega r + v_B \sin\phi) dS_0 \\ &= \int_0^R \int_0^{2\pi} p_0 r \left[\frac{\mu_s}{\theta \sqrt{\omega^2 r^2 + 2 v_B \omega r \sin\phi + v_B^2}} + \sigma \right] \\ &\quad \times (\omega r + v_B \sin\phi) r d\phi dr \\ &= \frac{p_0 \mu_s}{\theta} \int_0^R \int_0^{2\pi} \frac{r^2 (\omega r + v_B \sin\phi)}{\sqrt{\omega^2 r^2 + 2 v_B \omega r \sin\phi + v_B^2}} d\phi dr \\ &\quad + \int_0^R p r^2 \sigma \int_0^{2\pi} (\omega r + v_B \sin\phi) d\phi dr \\ &= \frac{p_0 \mu_s}{\theta} E_1(v_B, \omega) + \frac{1}{2} \pi p_0 \sigma \omega R^4 \end{aligned} \tag{7}$$

where the integral $E_1(v_B,\omega)$ is defined as a function of v_B and ω as follows:

$$E_1(v_B,\omega) = \int_0^R \int_0^{2\pi} \frac{r^2(\omega r + v_B \sin\phi)}{\sqrt{\omega^2 r^2 + 2 v_B \omega r \sin\phi + v_B^2}} d\phi dr. \tag{8}$$

Since there is no closed-form for integral calculation (8), it is not easy to see the relationship between the friction torque and the polishing parameters. We can, however, compute (8) numerically. For normal CMP operations, $0 \le v_B \le 500$ ft/min, $0 \le \omega \le 80$ rpm. Fig. 7(a) shows an example of the integral $E_1(v_B,\omega)$ values for such a range.

For most CMP processes, pad speed v_B is fast and wafer carrier rotating speed ω is slow. Using (1), we can approximate $|\mathbf{v}_{\mathrm{rel}}|$ as

$$|\mathbf{v}_{\mathrm{rel}}| \approx \omega r \sin\phi + v_B. \tag{9}$$

Using (9), we can calculate the friction torque M^{s} as[2]

$$M^{\mathrm{s}} = \frac{1}{4} p_0 \pi R^4 \omega \left(\frac{\mu_s}{\theta v_B} + 2\sigma \right). \tag{10}$$

B. Roller Torque

The friction moment applied to the roller rotating axis can be calculated in the same fashion as for the spindle system (Fig. 2). The polishing pad is tensioned and the friction force is applied on the roller. We can calculate the friction force F_x passing along the pad movement direction and the roller friction moment M^{r} as follows:

$$\begin{aligned} F_x &= \int_{S_0} \delta F_x dS_0 = \int_{S_0} \delta \mathbf{F} \cdot \mathbf{i} dS_0 \\ &= \frac{p_0 \mu_s}{\theta} E_2(v_B,\omega) + \pi p_0 R^2 \sigma v_B \end{aligned} \tag{11}$$

$$M^{\mathrm{r}} = F_x R_r \tag{12}$$

where R_r is the roller radius and the integral $E_2(v_B,\omega)$ is defined as

$$E_2(v_B,\omega) = \int_0^R \int_0^{2\pi} \frac{r(\omega r \sin\phi + v_B)}{\sqrt{\omega^2 r^2 + 2 v_B \omega r \sin\phi + v_B^2}} d\phi dr. \tag{13}$$

Similar to the integral $E_1(v_B,\omega)$, Fig. 7(b) shows an example of the integral $E_2(v_B,\omega)$ values for a normal CMP operation range. When the pad speed v_B is fast and the wafer carrier speed

[2]Detailed calculations can be found in the Appendix.

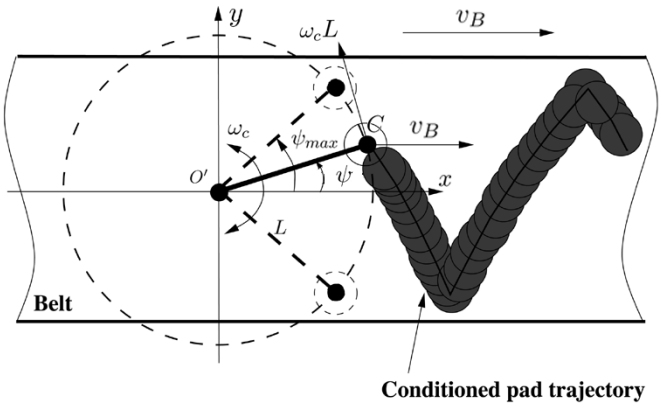

Fig. 8. Kinematics schematic of the radial arm conditioner.

ω is slow, using (9) we can obtain a similar approximation for (12)

$$M^{\mathrm{r}} = p_0 \pi R^2 R_r \left(\frac{\mu_s}{\theta} + \sigma v_B \right). \tag{14}$$

Remark 1: From Fig. 7, we can clearly see that integral $E_1(v_B,\omega) \ll E_2(v_B,\omega)$ for the same v_B and ω. Moreover, $E_1(v_B,\omega)$ is not sensitive to the wafer carrier speed changes at a large pad speed. Similarly, $E_2(v_B,\omega)$ is not sensitive to the pad speed changes since σ is small. Comparing (10) with (14), we can also obtain $M^{\mathrm{s}} \ll M^{\mathrm{r}}$. This fact is observed in experiments shown in the companion paper [9].

Remark 2: For most CMP processes, the calculations of the spindle and roller torques can be approximated by (10) and (14), respectively. The model parameter $\sigma = \sigma_2 - (\mu_s - \mu_c/\theta v_s)$ in most cases satisfies $0 \leq |\sigma| \ll 1$ because μ_c and μ_s are very close and $\theta > 1$.[3] Therefore, the spindle torque M^{s} is proportional to the external pressure p_0, the wafer carrier speed ω and the reciprocal of the pad speed v_B; the roller torque M^{r} is also proportional to the pressure p_0 but not sensitive to the wafer carrier speed ω and to the pad speed v_B (due to a small σ) at all. This theoretical conclusion has been verified by the experimental results presented in [9].

IV. Pad Conditioning Effect on Friction Models

A kinematic analysis of the conditioner disk movement on the polishing pad is important for studying the pad conditioning effects. Fig. 8 shows a kinematics diagram of the radial arm conditioner system. The radial arm of the conditioner rotates with constant angular speed ω_c around the fixed point O'. Denote the maximum angular displacement of the radial arm as $\psi_{\max}$. The movement of the conditioner disk is symmetric with respect to the center line of the polishing pad. Define an x-y coordinate system as shown in Fig. 8 and denote the arm length as L.

We neglect the time that the radial arm accelerates from 0 to ω_c and decelerates from ω_c to 0 at the front-limit and rear-limit positions.[4] Due to the periodic movement of the conditioner disk, we only need to study a two-sweep time period. Considering the moving trajectory of the conditioner disk center point C on the polishing pad, we can obtain the following velocity $v_C(t)$

$$\begin{cases} v_{C_x}(t) = v_B - \omega_c L \sin(\omega_c t) \\ v_{C_y}(t) = \omega_c L \cos(\omega_c t) \end{cases}. \tag{15}$$

Here we take counter-clockwise rotation as the positive angular velocity. The radial arm rotating angle $\psi(t) = \omega_c t$ must be within the range of the maximum value $\psi_{\max}$, i.e., $-\psi_{\max} \leq \psi(t) \leq \psi_{\max}$.

For the linear pad conditioning system, the trajectory of the conditioner disk center C on the pad is much easier to analyze since the motion of the conditioner disk is decoupled in the x- and y, axis directions. Similarly we can obtain the velocity of the point C as follows:

$$\begin{cases} v_{Cx}(t) = v_B \\ v_{Cy}(t) = \pm v_L \end{cases}. \tag{16}$$

Here, the velocity vector in the positive y axis direction takes a positive value. The conditioner disk position is restricted by $-L\sin(\psi_{\max}) \leq y_C(t) \leq L\sin(\psi_{\max})$.

Fig. 9(a) shows an example of the trajectories of the conditioner disk center point C on the polishing pad under both radial arm and linear conditioner systems. The pad speed is 200 ft/min, the time period per sweep is 7 s, $\psi_{\max} = 35°$, and $L = 10$in. From Fig. 9(a) we can clearly see that the trajectory difference between these two conditioner systems is not significant and, in fact, their trajectories are almost identical. This is because the pad speed is much faster than the conditioner sweep speed and the trajectory is dominated by the pad linear motion. In the following, we assume that the effects of both conditioner systems are the same and only analyze the linear conditioner system.

Without pad conditioning, the wafer/pad friction coefficients μ_s, μ_c are considered to be constants across the pad. Under pad conditioning, μ_s and μ_c are no longer constant and uniform across the pad since the conditioner disk changes the pad surface. The wafer/pad friction coefficients are different at various locations: for the portion of the pad that has been conditioned by the disk, the friction coefficients are higher than the portion that has not been conditioned.

Fig. 10 shows the kinematic relationship between a conditioned pad portion and the wafer. We denote the conditioner disk radius as r and the distance from the wafer center to the center of the conditioner disk as $h(t)$. During one conditioning sweep, the conditioned pad portion (shaded area in Fig. 10) moves across the wafer surface at a constant speed. For simplicity, we assume that the end-limit positions of conditioner disk are tangent with the wafer surface (as shown in Fig. 10). Then $h(t)$ is changing from $R+r$ (conditioner disk cutting into the wafer surface) to 0 (conditioner disk covering the wafer center portion) and then to $-(R+r)$ (conditioner disk leaving the wafer surface). In order to calculate the pad conditioning impact on friction forces and torques, we can first calculate the variations of the area of the conditioned pad portion as a function of time t.

Denote the period of the conditioner movement as T_c per sweep. Consider a two-sweep period when the conditioner disk

[3]Estimating model parameters such as σ and μ_s/θ will be discussed in [9].

[4]This assumption is valid since the driving direct current motor can accelerate and decelerate within a time less than 3% of the sweep time.

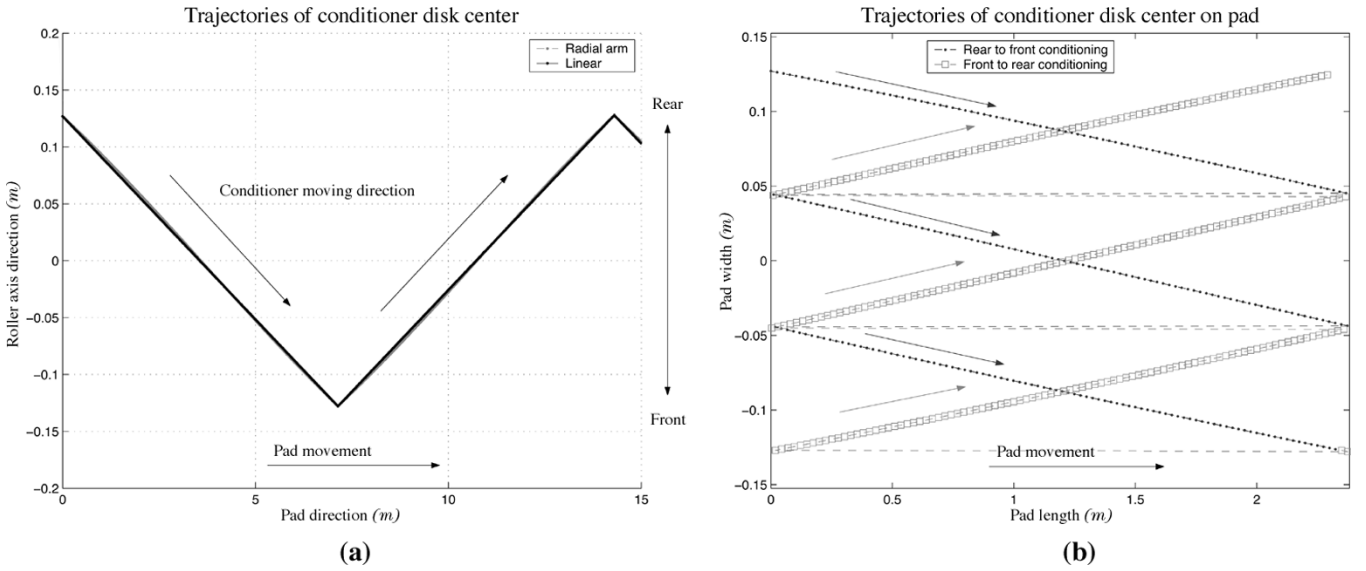

Fig. 9. Trajectories of conditioner disk center for a two-sweep conditioning system. (a) Trajectory of two conditioner systems on an infinitely-long polishing pad. (b) Trajectory of linear conditioner system on a 2.3-m-long polishing pad.

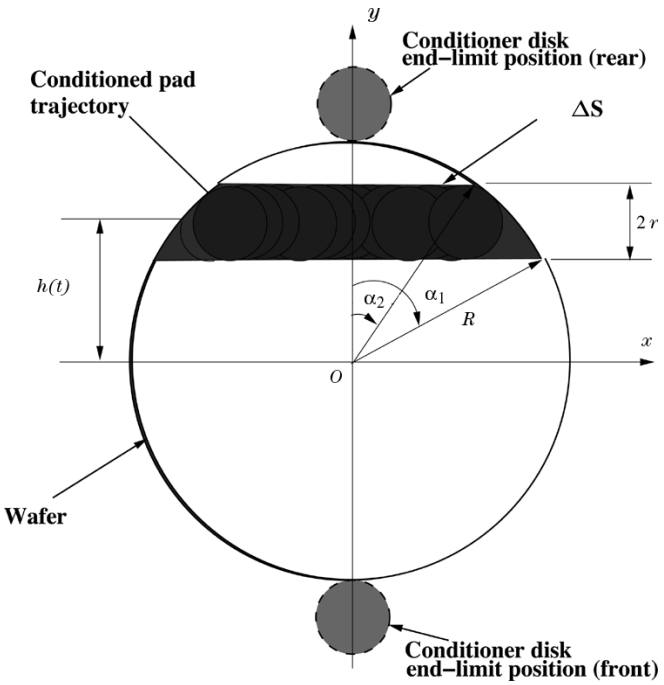

Fig. 10 . Spatial relationship between the conditioned pad portion and the wafer.

moves from the rear to the front and then back to the rear positions (2 sweeps). The conditioner disk center position $h(t)$ can be calculated as

$$h(t) = \begin{cases} (R+r) - v_c t, & \text{if } 0 \le t < T_c \\ -(R+r) + v_c(t - T_c), & \text{if } T_c \le t < 2T_c \end{cases} \quad (17)$$

where v_c is the linear moving velocity of the conditioner disk.

We assume that the pad linear motion dominates the relative velocity between the wafer and the pad. Therefore, the increased amount of friction forces due to pad conditioning can be calculated as a function of the fraction of the conditioned pad portion area (shaded area in Fig. 10) out of the whole wafer area. For the spindle friction torque, we have to consider both magnitude and sign of the shaded area with respect to the wafer center O. Let $\Delta\mathbf{S}^{\mathrm{s}}(t)$ denote the signed area of the conditioned pad portion within a rear-to-front conditioning sweep (i.e., $0 \le t < T_c$).[5] $\Delta\mathbf{S}^{\mathrm{s}}(t)$ can be calculated as follows (see (18) at bottom of the next page).[6]

We are now ready to estimate the difference in the friction torque with and without pad conditioning. Suppose that after pad conditioning the wafer/pad friction coefficients (both Coulomb and static friction coefficients) increase by the same amount $\gamma_\mu \ge 0$

$$\mu_{c_{\mathrm{cond}}} = (1+\gamma_\mu)\mu_c, \quad \mu_{s_{\mathrm{cond}}} = (1+\gamma_\mu)\mu_s$$

where $\mu_{c_{\mathrm{cond}}}$ and $\mu_{s_{\mathrm{cond}}}$ are the Coulomb and static wafer/pad friction coefficients after pad conditioning. Since the increase in friction coefficient only happens on the conditioned pad portion, the additional spindle moment due to pad conditioning is proportional to the fraction of the conditioned pad portion area. We can then obtain the following calculation for the spindle friction torque

$$\begin{aligned} M^{\mathrm{s}}_{\mathrm{cond}}(t) &= \left(1 + \gamma_\mu \frac{\Delta\mathbf{S}^{\mathrm{s}}(t)}{\pi R^2}\frac{|h(t)|}{R}\right) M^{\mathrm{s}} \\ &= \left(1 + \gamma_\mu \gamma^{\mathrm{s}}_{\mathrm{cond}}(t)\right) M^{\mathrm{s}}, \quad t \in [0, T_c) \end{aligned} \quad (19)$$

where $\gamma^{\mathrm{s}}_{\mathrm{cond}}(t) = (\Delta\mathbf{S}^{\mathrm{s}}(t)|h(t)|/\pi R^3)$ is the pad conditioning factor at time t.

In (19), we only consider the effect of one conditioned pad trajectory within one pad rotating cycle. For a CMP process, the polishing pad is running at high speed and the conditioner sweep speed is relatively slow. In one conditioning sweep, the

[5]Due to symmetry, we can obtain a similar formula for $T_c \le t < 2T_c$.

[6]In practice, v_c is calculated as $v_c = (2R + \delta/T_c)$, where $\delta \ge 0$ and T_c is specified by users. Therefore, $v_c T_c \ge 2R$. The relationship $R \ge 3r$ holds for the LPT systems.

conditioned pad trajectory could repeatedly cross the wafer surface several times (see Fig. 9(b), for example.) In order to capture the effect of multiple pad rotating cycles, we need to modify $\Delta\mathbf{S}^{\mathrm{s}}(t)$ in (19) as

$$\Delta\mathbf{S}^{\mathrm{s}}_{e}(t) = \Delta\mathbf{S}^{\mathrm{s}}(t) + \sum_{i=1}^{N} \beta_i \Delta\mathbf{S}^{\mathrm{s}}(t - iT_B) \tag{20}$$

where $0 < \beta_i < 1, i = 1, \ldots, N$, are the forgetting factors, and N is the number of pad rotating cycles within one pad conditioning sweep, $1 \le N \le [v_B T_c / L_B]$,[7] where L_B is the length of the polishing pad. Time constant T_B is defined as the time period for the conditioned pad trajectory to travel one pad length ($T_B = L_B / v_B$).[8] The values of the forgetting factors β_i depend on the polishing and conditioner systems and in practice we determine these values empirically.

For the roller system moment, we can calculate the effect of pad conditioning in the same fashion. One difference is that the pad conditioning effect always adds an amount of extra positive load on the roller axis while for the spindle moment the extra load could be either positive or negative. Therefore, we can obtain an unsigned area $\Delta\mathbf{S}^{\mathrm{r}}(t)$ (instead of signed area $\Delta\mathbf{S}^{\mathrm{s}}(t)$ for the spindle system) of the conditioned pad portion (shaded area in Fig. 10) as (see (21) at bottom of page) We can modify (19) and (20) accordingly for the roller system and a similar factor $\gamma^{\mathrm{r}}_{\mathrm{cond}}$ can be obtained to model the pad conditioning impact.

We neglect the friction force that the conditioner disk applies on the polishing pad since this amount of force is much smaller than the wafer/pad friction force. With the pad conditioning factor $\gamma^{r}_{\mathrm{cond}}(t)$, we can obtain the roller system moment $M^{\mathrm{r}}_{\mathrm{cond}}$ with respect to the roller rotating axis as

$$M^{\mathrm{r}}_{\mathrm{cond}}(t) = (1 + \gamma_\mu \gamma^{r}_{\mathrm{cond}}(t))\, M^{\mathrm{r}} \tag{22}$$

where $\gamma^{\mathrm{r}}_{\mathrm{cond}}(t) = (\Delta\mathbf{S}^{\mathrm{r}}(t)/\pi R^2)$.

Fig. 11 shows one example of the spindle pad conditioning factors $\gamma^{\mathrm{s}}_{\mathrm{cond}}(t)$ and roller pad conditioning factor $\gamma^{\mathrm{r}}_{\mathrm{cond}}(t)$, respectively. In the calculation, we use $\beta_1 = 0.6$, $\beta_2 = 0.3$ ($N = 2$), $T_c = 7$ sec, $v_B = 200$ ft/min, and $L_B = 2.38$ m. From Fig. 11 we notice different pad conditioning effects on the spindle and roller moments. For both spindle and roller systems, the extra friction moment fluctuations due to pad conditioning look like sinusoid curves. However, for the spindle system, the oscillation period is about $2T_c$ around zero while for the roller system the period is T_c and always positive.

V. Patterned Wafer Topography Effect

In this section, we consider how the patterned wafer film topography affects friction modeling. Since the local wafer/pad contact pressure decreases during the patterned wafer polishing process, the friction forces between the patterned wafer and pad

[7]The function $[x]$ means the largest integer number that is less than a real number $x \in \mathbb{R}$.

[8]There are in total T_c/T_B conditioned pad trajectories on the polishing pad during one conditioning sweep. It is easy to see that if the number $v_B T_c / L_B$ is an irrational number, the conditioner disk will cover the whole pad surface by a large number of sweeps.

$$\Delta\mathbf{S}^{\mathrm{s}}(t) = \begin{cases} R^2\left[\cos^{-1}\left(\frac{h-r}{R}\right) - \frac{h-r}{R}\sqrt{1-\frac{(h-r)^2}{R^2}}\right] & \text{if } 0 \le t < \frac{2r}{v_c} \\ R^2\left\{\cos^{-1}\left(\frac{h-r}{R}\right) - \cos^{-1}\left(\frac{h+r}{R}\right)\right. & \\ \quad \left. -\frac{1}{R}\left[(h-r)\sqrt{1-\frac{(h-r)^2}{R^2}} - (h+r)\sqrt{1-\frac{(h+r)^2}{R^2}}\right]\right\} & \text{if } \frac{2r}{v_c} \le t < \frac{R}{v_c} \\ R^2\left\{\cos^{-1}\left(\frac{r-h}{R}\right) - \cos^{-1}\left(\frac{h+r}{R}\right)\right. & \\ \quad \left. -\frac{1}{R}\left[(r-h)\sqrt{1-\frac{(h-r)^2}{R^2}} - (h+r)\sqrt{1-\frac{(h+r)^2}{R^2}}\right]\right\} & \text{if } \frac{R}{v_c} \le t < \frac{R+2r}{v_c} \\ -R^2\left\{\cos^{-1}\left(\frac{|h|-r}{R}\right) - \cos^{-1}\left(\frac{|h|+r}{R}\right)\right. & \\ \quad \left. -\frac{1}{R}\left[(|h|-r)\sqrt{1-\frac{(|h|-r)^2}{R^2}} - (|h|+r)\sqrt{1-\frac{(|h|+r)^2}{R^2}}\right]\right\} & \text{if } \frac{R+2r}{v_c} \le t < \frac{2R-r}{v_c} \\ -R^2\left[\cos^{-1}\left(\frac{|h|-r}{R}\right) - \frac{|h|-r}{R}\sqrt{1-\frac{(|h|-r)^2}{R^2}}\right] & \text{if } \frac{2R-r}{v_c} \le t < T_c \end{cases} \tag{18}$$

$$\Delta\mathbf{S}^{\mathrm{r}}(t) = \begin{cases} R^2\left[\cos^{-1}\left(\frac{|h|-r}{R}\right) - \frac{|h|-r}{R}\sqrt{1-\frac{(|h|-r)^2}{R^2}}\right] & \text{if } 0 \le t < \frac{2r}{v_c} \text{ or } \frac{2R-r}{v_c} \le t < T_c \\ R^2\left\{\cos^{-1}\left(\frac{|h|-r}{R}\right) - \cos^{-1}\left(\frac{|h|+r}{R}\right)\right. & \\ \quad \left. -\frac{1}{R}\left[(|h|-r)\sqrt{1-\frac{(|h|-r)^2}{R^2}} - (|h|+r)\sqrt{1-\frac{(|h|+r)^2}{R^2}}\right]\right\} & \text{if } \frac{2r}{v_c} \le t < \frac{R}{v_c} \text{ or } \frac{R+2r}{v_c} \le t < \frac{2R-r}{v_c} \\ R^2\left\{\pi - \left[\cos^{-1}\left(\frac{r+h}{R}\right) - \cos^{-1}\left(\frac{r-h}{R}\right)\right]\right. & \\ \quad \left. +\frac{1}{R}\left[(r+h)\sqrt{1-\frac{(h+r)^2}{R^2}} - (h-r)\sqrt{1-\frac{(h-r)^2}{R^2}}\right]\right\} & \text{if } \frac{R}{v_c} \le t < \frac{R+2r}{v_c} \end{cases} \tag{21}$$

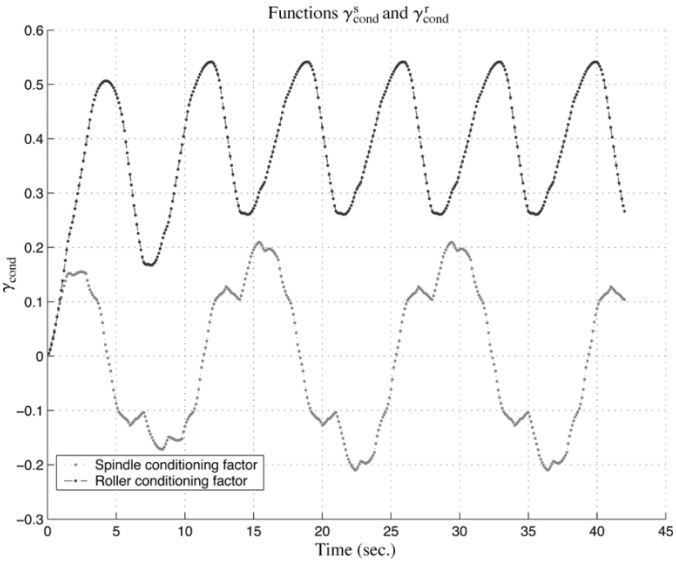

Fig. 11. Example of the friction torque factor $\gamma_{\rm cond}(t)$ under two sweep pad conditioning.

also decrease. At the beginning of the polishing process, the local wafer/pad contact pressure $p = \delta F_n$ is higher than the external pressure p_0 because the wafer/pad contact area S is much smaller than the wafer disk area S_0. Assume that all dies on the wafer are identical and then we can obtain the average pressure δF_n as

$$\delta F_n = \frac{p_0 S_0}{S}. \tag{23}$$

In the following, we use the shallow trench isolation (STI) device patterned wafers as an example to explain how we calculate the pattern factor $\gamma_{\rm patt}(t)$. Fig. 12(a) shows the schematic of the STI device cross section. In the STI process, isolation trenches are plasma etched in the silicon, and then overfilled with chemical vapor deposition (CVD) silicon dioxide. Next, the oxide is polished back to a planar surface using CMP, while removing as little of the nitride as possible. Fig. 12 shows the snapshot sequence of surface topography cross section changes of an STI CMP process. Let L_0 and L_A denote the pitch and active film widths, respectively.[9] The pattern density ρ is defined as the ratio of trench width over the whole pitch width

$$\rho = \frac{L_0 - L_A}{L_0} = 1 - \frac{L_A}{L_0}. \tag{24}$$

Denote the initial trench step height as h_{S_0} [Fig. 12(a)]. Let h_c denote the contact height at which the polishing pad starts to touch the trench oxide surface [Fig. 12(b)]. When the process starts [Fig. 12(a)], the pad only contacts the active oxide area and the bottom of the trench is never polished (assuming $h_{S_0} \geq h_c$). Therefore, the wafer/pad contact area S is equal to the total active oxide area across the wafer. When more oxide materials have been removed from the surface, the step height h_S decreases and under the pressure p_0 the pad will start to touch the trench oxide, as shown in Fig. 12(b). Once the process continues, the contact area S keeps increasing [as shown in Fig. 12(c)]. Finally, the active oxide area is completely removed (step height $h_S = 0$) and the wafer/pad contact area is the whole wafer surface, namely $S = S_0$ [Fig. 12(d)].

We consider the step height h_S model by Smith *et al.* [19] and Lee [20].

Case 1: $h_c \leq h_{S_0}$

In this case, the pad does not contact the trench oxide at the beginning of the polishing process. The step height $h_S(t)$ during the polishing process can be modeled as

$$h_S(t) = \begin{cases} h_{S_0} - \frac{RR_B}{\rho} t, & 0 \leq t < t_c \\ h_c e^{-\frac{t-t_c}{\tau_B}}, & t \geq t_c \end{cases} \tag{25}$$

where RR_B is the blanket oxide wafer removal rate, t_c is the time when the step height h_S reaches the contact height h_c and $\tau_B = (\rho h_c / RR_B)$ is the delaying constant for film height.

For the wafer/pad contact area S, it is easy to see that during $t < t_c$, $S = S_0(1-\rho)$, and $S \to S_0$ as $t \to \infty$; for the transient period $t \geq t_c$ we have to calculate the contact area between the polishing pad and the oxide trench [Fig. 12(c)]. Let S_P denote one pitch area and S_T and S_c denote the contact areas of the polishing pad with the oxide trench and with a pitch, respectively. Denote the trench length as l_0. We have $S_P = l_0 L_0$ and the trench contact area S_T can be calculated as

$$\begin{aligned} S_T &= 2l_0 \left(h_c - h_S(t)\right) \tan\alpha = 2l_0 \left[h_c - h_S(t)\right] \frac{L_0 - L_A}{2h_c} \\ &= \frac{l_0 \left[h_c - h_S(t)\right] (L_0 - L_A)}{h_c}, \quad t \geq t_c. \end{aligned} \tag{26}$$

Substituting (25) into the above equation, we can obtain

$$S_T = S_P \rho \left(1 - e^{-\frac{t-t_c}{\tau_B}}\right), \quad t \geq t_c. \tag{27}$$

Therefore, the total wafer/pad contact area within a pitch S_c is then given as

$$S_c = S_T + S_P(1-\rho) = S_P \left(1 - \rho e^{-\frac{t-t_c}{\tau_B}}\right).$$

For the same density and pitch width,[10] $\rho(x,y) = \rho$, $L_0(x,y) = L_0$, we then have a uniform polishing profile across the wafer. The pattern factor $\gamma_{\rm patt}(t)$ is then calculated as

$$\gamma_{\rm patt}(t) = \frac{S_0}{S} = \frac{S_P}{S_c} = \begin{cases} \frac{1}{1-\rho}, & 0 \leq t < t_c \\ \frac{1}{1-\rho e^{-\frac{t-t_c}{\tau_B}}}, & t \geq t_c. \end{cases} \tag{28}$$

Case II: $h_c > h_{S_0}$

In this case, the pad already touches the down trench area when the polishing starts. The de-

[9] A pitch area consists of a trench and an active area [Fig. 12(a)].

[10] We will discuss how to calculate the pattern factor $\gamma_{\rm patt}(t)$ with various densities in a die in [9].

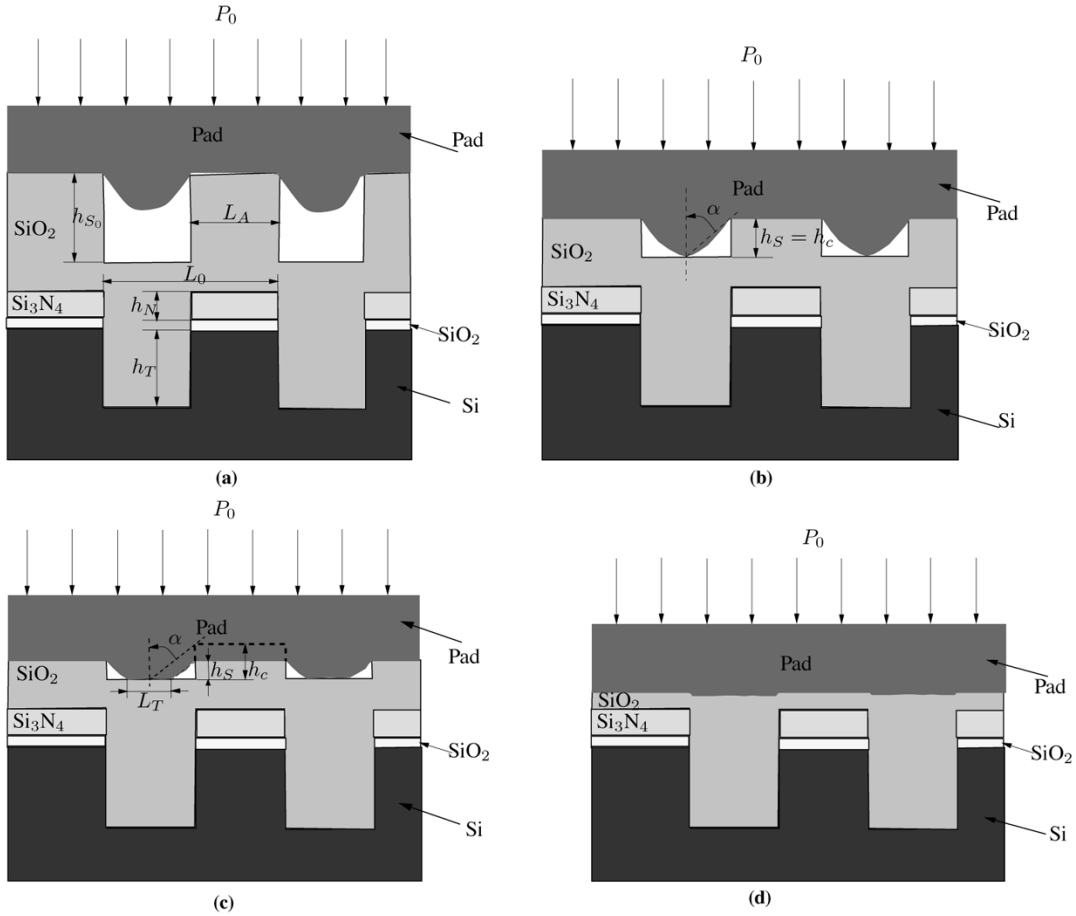

Fig. 12. Snapshot schematic of STI patterned wafer surface cross section during a CMP process: (a) starting polishing; (b) at contact height; (c) pad touchdown with trenches; and (d) surface planarized.

crease of the step height $h_S(t)$ during the polishing process can be modeled as

$$h_S(t) = h_{S_0} e^{-\frac{t}{\tau_B}}. \tag{29}$$

From (26) and (29), we have

$$\frac{dS_T}{dt} = -\frac{S_P \rho}{h_c}\frac{dh_S}{dt} = \frac{S_P \rho h_{S_0}}{h_c \tau_B} e^{-\frac{t}{\tau_B}}. \tag{30}$$

We can solve (30) with the initial condition $S_T(0) = S_P\rho(1 - (h_{S_0}/h_c))$

$$S_T(t) = S_P \rho \left(1 - \frac{h_{S_0}}{h_c} e^{-\frac{t}{\tau_B}}\right). \tag{31}$$

Similarly, we can calculate the pattern factor γ_{patt} as

$$\gamma_{\text{patt}}(t) = \frac{S_0}{S} = \frac{S_P}{S_c} = \frac{1}{1 - \frac{h_{S_0}}{h_c}\rho e^{-\frac{t}{\tau_B}}}. \tag{32}$$

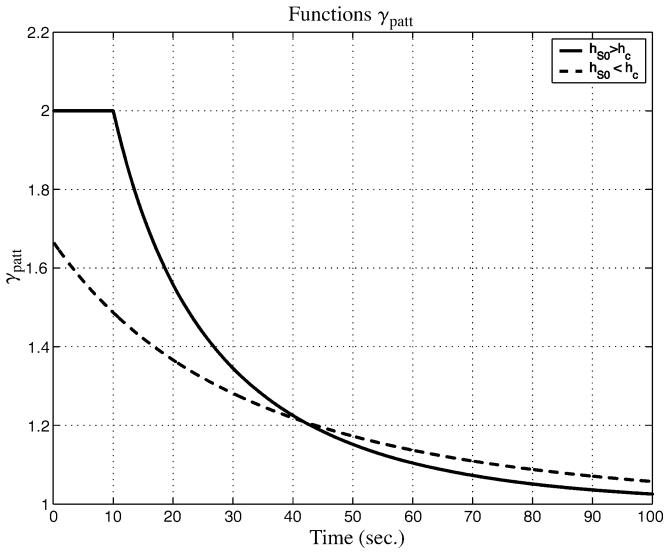

Fig. 13. Example of the friction torque factor $\gamma_{\text{patt}}(t)$ with STI patterned wafers with two different contact heights h_c.

Fig. 13 shows one example of the STI patterned wafer friction factor $\gamma_{\text{patt}}(t)$. The following parameters are used in the example: $\rho = 50\%$, $RR_B = 3000$ Å/min, and $h_{S_0} = 4000$ Å. Two contact heights are used to plot γ_{patt}: $h_c = 3000$ Å and $h_c = 5000$ Å. For a larger initial step height ($h_{S_0} > h_c$), the contact area is smaller since the pad only contacts the active oxide area at the beginning of the process. Therefore, the friction factor is larger (solid line in Fig. 13). On the other hand, if the initial step height is small ($h_{S_0} < h_c$), the friction factor γ_{patt} is smaller since the pad contacts the wafer on both the active oxide and down trench areas.

For both cases, the wafer/pad contact area S and the average wafer/pad pressure $p(t)$ can be estimated as

$$S(t) = \frac{S_0}{\gamma_{\rm patt}(t)}, \quad \text{and} \quad p(t) = \delta F_n = p_0 \gamma_{\rm patt}(t). \tag{33}$$

Therefore, for patterned wafer polishing with pad conditioning, the spindle and roller moments can be modified based on (19) and (22) as

$$\begin{aligned} M^{\rm s}_{\rm patt}(t) &= \gamma_{\rm patt}(t)\left[1+\gamma_\mu \gamma^{\rm s}_{\rm cond}(t)\right] M^{\rm s} \\ M^{\rm r}_{\rm patt}(t) &= \gamma_{\rm patt}(t)\left[1+\gamma_\mu \gamma^{r}_{\rm cond}(t)\right] M^{\rm r}. \end{aligned} \tag{34}$$

VI. Conclusion

A wafer/pad friction modeling, estimation, and monitoring scheme is proposed for CMP processes. Analytical friction modeling is discussed in this paper and experimental validation and applications will be presented in the companion paper [9]. In this paper, the kinematic relationship between the wafer and the polishing pad was first investigated. A distributed LuGre dynamic friction model was used to model the wafer/pad friction characteristic. Since it is difficult to measure the wafer/pad friction directly, the use of the polisher spindle and roller moments to monitor the friction *in situ* was instead proposed. An analytical relationship between wafer/pad friction coefficients, polishing parameters and spindle and roller moments has been proposed. Moreover, the effects of pad conditioning and patterned wafer topography on the wafer/pad friction characteristic were also investigated. The results showed that the spindle torque is relatively small at high pad speeds typically used in practice. Roller motor torque is instead a potential candidate to be used to monitor the wafer/pad friction and the pad conditioning system as well as other polishing parameters such as wafer carrier pressure. The proposed models can be used to monitor *in situ* the wafer/pad friction and further used as a tool for system diagnostics and process control. The friction modeling and analysis method discussed in this paper can also be extended and applied to orbit and rotary CMP polishers.

Appendix
Calculation of Moment $M^{\rm s}$ With a Fast Pad Speed v_B and a Slow Wafer Carrier Speed ω

By approximation (9), the magnitude of the spindle moment $M^{\rm s}$ is calculated as

$$\begin{aligned} M^{\rm s} &= \int_S pr\left[\frac{\mu_s}{\theta|\mathbf{v}_{\rm rel}|}+\sigma\right](\omega r + v_B\sin\phi)dS \\ &= \int_0^R\int_0^{2\pi} pr\left[\frac{\mu_s}{\theta(\omega r\sin\phi+v_B)}+\sigma\right] \\ &\quad \times(\omega r+v_B\sin\phi)r d\phi dr \\ &= \int_0^R \frac{pr^2\mu_s}{\theta}\int_0^{2\pi}\frac{\omega r+v_B\sin\phi}{\omega r\sin\phi+v_B}d\phi dr \\ &\quad + \int_0^R pr^2\sigma\int_0^{2\pi}(\omega r+v_B\sin\phi)d\phi dr. \end{aligned} \tag{35}$$

Define $\xi = (\omega r/v_B)$ and we can calculate the first integral term in the above equation as

$$\begin{aligned} &\int_0^R \frac{pr^2\mu_s}{\theta}\int_0^{2\pi}\frac{\omega r+v_B\sin\phi}{\omega r\sin\phi+v_B}d\phi dr \\ &\quad = \int_0^R \frac{pr\mu_s}{\theta}\int_0^{2\pi}\frac{\xi+\sin\phi}{\xi\sin\phi+1}d\phi dr \\ &\quad = \int_0^R \frac{pr^2\mu_s}{\theta}\frac{2\pi}{\xi}(1-\sqrt{1-\xi^2})d\phi dr \\ &\quad \approx \int_0^R \frac{pr^2\mu_s}{\theta}\frac{2\pi}{\xi}\left[1-\left(1-\frac{1}{2}\xi^2\right)\right]d\phi dr \\ &\quad = \int_0^R \frac{pr^2\mu_s}{\theta}\pi\xi dr \end{aligned} \tag{36}$$

where we use the fact $(1-\xi^2)^{1/2}\approx 1-(1/2)\xi^2$ since $0<\xi\ll 1$. Combining (35) and (36), we obtain the friction moments (10) as

$$\begin{aligned} M^{\rm s} &= \int_0^R pr^2\frac{\mu_s}{\theta}\frac{\pi}{v_B}\omega r dr + \int_0^R pr^2\int_0^{2\pi}\sigma(\omega r+v_B\sin\phi)d\phi dr \\ &= \frac{1}{4}\pi p R^4\omega\left(\frac{\mu_s}{\theta v_B}+2\sigma\right). \end{aligned}$$

Acknowledgment

The author thanks Dr. G. Fu and Dr. R. Krisler at Lam Research Corporation for various helpful discussions.

References

[1] D. Wang, J. Lee, K. Holland, T. Bibby, S. Beaudoin, and T. Cale, "Von Mises stress in chemical-mechanical polishing processes," *J. Electrochem. Soc.*, vol. 144, no. 3, pp. 1121–1127, 1997.

[2] G. Fu, A. Chandra, S. Guha, and G. Subhash, "A plasticity-based model of material removal in Chemical-Mechanical Polishing (CMP)," *IEEE Trans. Semicond. Manuf.*, vol. 14, no. 4, pp. 406–417, Nov. 2001.

[3] S. R. Runnels and L. M. Eyman, "Tribology analysis of chemical-mechanical polishing," *J. Electrochem. Soc.*, vol. 141, no. 6, pp. 1698–1701, 1994.

[4] S. Sundararajan, D. G. Thakurta, D. W. Schwendeman, S. P. Murarka, and W. N. Gill, "Two-dimensional wafer-scale chemical mechanical planarization models based on lubrication theory and mass transport," *J. Electrochem. Soc.*, vol. 146, no. 2, pp. 761–766, 1999.

[5] C. H. Cho, S. S. Park, and Y. Ahn, "Three-dimensional wafer scale hydrodynamic modeling for chemical mechanical polishing," *Thin Solid Films*, vol. 389, pp. 254–260, 2001.

[6] D. G. Thakurta, C. L. Borst, D. W. Schwendeman, R. J. Gutmann, and W. N. Gill, "Pad porosity, compressibility and slurry delivery effects in chemical-mechanical planarization: Modeling and experiments," *Thin Solid Films*, vol. 366, pp. 181–190, 2000.

[7] J. Tichy, J. A. Levert, L. Shan, and S. Danyluk, "Contact mechanics and lubrication hydrodynamics of chemical mechanical polishing," *J. Electrochem. Soc.*, vol. 146, no. 4, pp. 1523–1528, 1999.

[8] Y. Moon, "Mechanical aspects of the material removal mechanism in chemical mechanical polishing (CMP)," Ph.D. dissertation, Dept. Mechanical Eng., Univ. California, Berkeley, 1999.

[9] J. Yi, "On the wafer/pad friction of chemical–mechanical planarization (CMP) processes—Part II: Experiments and applications," *IEEE Trans. Semicond. Manuf.*, vol. 18, no. 3, pp. 371–383, Aug. 2005.

[10] T. Bibby and K. Holland, "Endpoint detection for CMP," *J. Electron. Mater.*, vol. 27, no. 10, pp. 1073–1081, 1998.
[11] D. L. Hetherington and D. J. Stein, "Recent advances in endpoint and in-line monitoring techniques for chemical-mechanical polishing processes," in *Proc. CMP-MIC Conf.*, Santa Clara, CA, 2001, pp. 315–323.
[12] H. Litvak and H. M. Tzeng, "Implementing real-time endpoint control in CMP," *Semicond. Int.*, vol. 19, no. 8, pp. 259–264, 1996.
[13] A. K. Sikder, F. Giglio, J. Wood, A. Kumar, and M. Anthony, "Optimization of tribological properties of silicon dioxide during the chemical mechanical planarization process," *J. Electron. Mater.*, vol. 30, no. 12, pp. 1520–1526, 2001.
[14] Y. Homma, K. Fukushima, S. Kondo, and N. Sakuma, "Effects of mechanical parameters on CMP characteristics analyzed by two-dimensional frictional-force measurement," *J. Electrochem. Soc.*, vol. 150, no. 12, pp. G751–G757, 2003.
[15] A. Jensen, P. Renteln, S. Jew, C. Raeder, and P. Cheung, "Empirical-based modeling for control of CMP removal uniformity," *Solid State Technol.*, vol. 44, no. 6, pp. 101–106, 2001.
[16] T. Dyer and J. Schlueter, "Characterizing CMP pad conditioning using diamond abrasives," *MICRO*, Jan. 2002.
[17] J. Luo and D. A. Dornfeld, "Material removal mechanism in chemical mechanical polishing: theory and modeling," *IEEE Trans. Semicond. Manuf.*, vol. 14, no. 2, pp. 112–133, May 2001.
[18] C. Canudas de Wit, H. Olsson, K. J. Åström, and P. Lischinsky, "A new model for control of systems with friction," *IEEE Trans. Autom. Control*, vol. 40, no. 3, pp. 419–425, Mar. 1995.
[19] T. H. Smith, S. J. Fang, D. S. Boning, G. B. Shinm, and J. A. Stefani, "A CMP model combining density and time dependencies," in *Proc. CMP-MIC Conf.*, Santa Clara, CA, 1999, pp. 97–104.
[20] B. Lee, "Modeling of chemical mechanical polishing for shallow trench isolation," Ph.D. dissertation, Dept. Elect. Eng. Comp. Sci., Massachusetts Inst. Technol., Cambridge, MA, 2002.

Jingang Yi (S'99–A'02–M'02) was born in Hubei Province, China. He received the B.S. degree in electrical engineering from the Zhejiang University, Hangzhou, China, in 1993, the M.Eng. degree in precision instruments from Tsinghua University, Beijing, China, in 1996, the M.A. degree in applied mathematics, and the Ph.D. degree in mechanical engineering from the University of California, Berkeley, in 2001 and 2002, respectively.

From May 2002 to January 2005, he was with Lam Research Corporation, Fremont, CA, as a Systems Engineer. Since January 2005, he has been with Department of Mechanical Engineering, Texas A&M University, College Station, as a Visiting Assistant Professor. His research interests include intelligent and autonomous systems, mechatronics, automation science, and engineering with applications to semiconductor manufacturing and intelligent transportation systems.

Dr. Yi is the recipient of the Kayamori Best Paper Award of the 2005 IEEE Conference on Robotics and Automation (ICRA).